

# First-Principles Nonadiabatic Dynamics Simulation of Azobenzene Photodynamics in Solutions

Ruabin Liang\*

Cite This: <https://doi.org/10.1021/acs.jctc.1c00105>

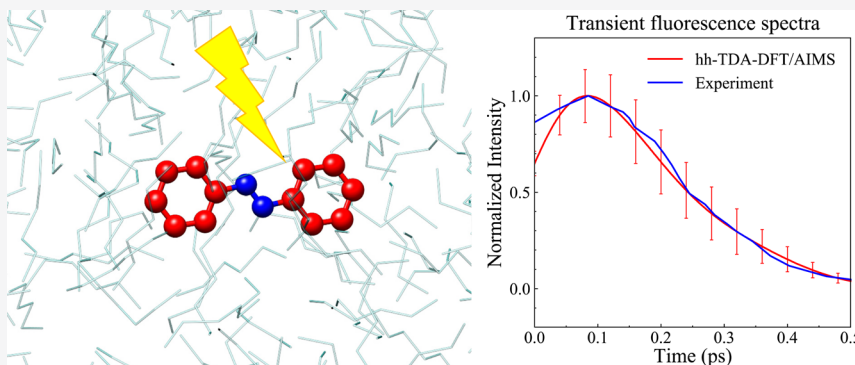
Read Online

ACCESS |

Metrics &amp; More

Article Recommendations

Supporting Information



**ABSTRACT:** The photoisomerization of azobenzene is a prototypical reaction of various light-activated processes in material and biomedical sciences. However, its reaction mechanism has been under debate for decades, partly due to the challenges in computational simulations to accurately describe the molecule's photodynamics. A recent study (*J. Am. Chem. Soc.* **2020**, *142* (49), 20,680–20,690) addressed the challenges by combining the hole–hole Tamm–Dancoff Approximated (hh-TDA) density functional theory (DFT) method with the ab initio multiple spawning (AIMS) algorithm. The hh-TDA-DFT/AIMS method was applied to first-principles nonadiabatic dynamics simulation of azobenzene's photodynamics in the vacuum. However, it remains necessary to benchmark this new method in realistic molecular environments against experimental data. In the current work, the hh-TDA-DFT/AIMS method was employed in a quantum mechanics/molecular mechanics setting to characterize the *trans* azobenzene's photodynamics in explicit methanol and *n*-hexane solvents, following both the  $S_1$  ( $n\pi^*$ ) and  $S_2$  ( $\pi\pi^*$ ) excitations. The simulated absorption and fluorescence spectra following the  $S_2$  excitation quantitatively agree with the experiments. However, the hh-TDA-DFT method overestimates the torsional barrier on the  $S_1$  state, leading to an overestimation of the  $S_1$  state lifetime. The excited-state population decays to the ground state through two competing channels. The reactive channel partially yields the *cis* azobenzene photoproduct, and the unreactive channel exclusively leads to the reactant. The  $S_2$  excitation increases the decay through the unreactive channel and thus decreases the isomerization quantum yield compared to the  $S_1$  excitation. The solvent slows down the azobenzene's torsional dynamics on the  $S_1$  state, but its polarity minimally affects the reaction kinetics and quantum yields. Interestingly, the dynamics of the central torsion and angles of azobenzene play a critical role in determining the final isomer of the azobenzene. This benchmark study validates the hh-TDA-DFT/AIMS method's accuracy for simulating the azobenzene's photodynamics in realistic molecular environments.

## INTRODUCTION

Azobenzene is a prototypical molecule for molecular photo-switches. Chemical modifications on azobenzene enable the fine tuning of its photochemical and photophysical properties, which has led to the design of photoresponsive molecular systems in various applications.<sup>1–3</sup> Despite the importance of this molecule, it remains challenging to fully understand its ultrafast photodynamics, especially its wavelength-dependent isomerization quantum yield. The quantum yield following the symmetry-forbidden  $S_1$  ( $n\pi^*$ ) excitation (0.2–0.3) is almost twice of that following the symmetry-allowed  $S_2$  ( $\pi\pi^*$ ) excitation (0.1–0.15).<sup>4–9</sup> Molecular simulation provides unique advantages in understanding azobenzene's photodynamics due

to its capability to reveal the reaction mechanism with full dynamical details at atomistic-level resolution. However, there are several challenges for simulation to correctly predict azobenzene's photodynamics. First, we need to accurately describe the potential energy surfaces (PESs) of multiple

Received: January 29, 2021

electronic states. Second, we need to accurately propagate the multistate nuclear wavefunctions according to the time-dependent Schrödinger equation. A recent study<sup>10</sup> addressed these challenges by first-principles nonadiabatic dynamics simulation. It combined the hole–hole Tamm–Dancoff approximated (hh-TDA) density functional theory (DFT) method<sup>11,12</sup> and the ab initio multiple spawning (AIMS) method<sup>13–15</sup> to characterize the photodynamics of azobenzene in the vacuum.<sup>10</sup> The hh-TDA-DFT method is a highly efficient first-principles electronic structure method that incorporates both static and dynamic electron correlations.<sup>11,12</sup> It accurately describes azobenzene's PES from the S<sub>0</sub> to the S<sub>2</sub> state.<sup>12</sup> Accordingly, the hh-TDA-DFT/AIMS simulation correctly predicted the wavelength-dependent isomerization quantum yield and revealed its underlying molecular mechanism.<sup>10</sup> The study<sup>10</sup> confirmed previous studies' findings based on the semiempirical nonadiabatic dynamics simulations,<sup>16–21</sup> PES calculations,<sup>22–25</sup> and single-state adiabatic dynamics simulations.<sup>26</sup> Furthermore, it revealed new reaction pathways on both the S<sub>1</sub> and S<sub>2</sub> excited states.<sup>10</sup>

Although the hh-TDA-DFT/AIMS method has achieved high accuracy in describing the azobenzene photodynamics in the vacuum, it is well-known that the molecular environments could largely change the kinetics, pathway, and quantum yield of the chemical reactions.<sup>27–32</sup> Therefore, it remains necessary to benchmark the new method's performance in realistic molecular environments against experimental observables, such as the absorption and fluorescence spectra. Moreover, to the best of my knowledge, only two semiempirical computational studies have investigated the azobenzene's photodynamics in solutions.<sup>20,21</sup> What is more, there have been few ab initio nonadiabatic dynamics simulations of such a system. Recent studies highlighted the importance of using correlated ab initio electronic structure methods for an accurate description of the azobenzene's PES.<sup>22,23</sup> To fill this void, this work benchmarks the hh-TDA-DFT/AIMS method for the *trans* azobenzene's (TAB) photodynamics in explicit solvents. To investigate the effect of the solvent's polarity on the TAB's photodynamics, two solvents with different dielectric constants were chosen: *n*-hexane and methanol. In each of the solvent system, the TAB's photodynamics following both the S<sub>1</sub> and S<sub>2</sub> excitations were simulated. The solvent slows down the S<sub>1</sub> state dynamics, but its polarity does not significantly change the photodynamics. The dynamics of the central torsion and angles of azobenzene play a critical role in determining the eventual photoproduct of the reaction.

## METHODS

This section describes the procedures for preparing, performing, and analyzing the AIMS simulations.

**Preparations of the AIMS Simulation.** It is well-known that the choice of initial condition (IC), i.e., the initial coordinates and momenta for all the atoms in the system, affects the results of nonadiabatic dynamics simulation. Therefore, special care is needed to prepare the ICs. To this end, the following procedure developed by Lischka et al.<sup>33–37</sup> was employed in the current work. In short, the procedure consists of the following steps:

(i) Classical sampling of solvent configurations using molecular mechanics (MM) molecular dynamics (MD) simulation while keeping the solute fixed at the gas-phase equilibrium structure. Snapshots selected from the MD trajectories contain different solvent configurations.

(ii) Wigner sampling of the isolated solute molecule based on the vibrational mode analysis using the quantum mechanics (QM) method. The vibrational modes of the solute are displaced, and the zero-point-energy (ZPE) is included in this step.

(iii) Replacing the solute structure in the MM MD trajectory snapshots with the structures sampled from the Wigner distribution in step (ii).

(iv) Re-thermalization of the solvent molecules with ground-state QM/MM MD simulation while fixing the coordinates of the solute. The coordinates and the velocities of the solvent molecules are sampled from Boltzmann distribution. The overlaps between the displaced solute molecule and the solvent molecules are reduced at the QM/MM level of theory in this step.

In this approach, the gas-phase Wigner sampling of azobenzene was combined with the Boltzmann sampling of the solvent molecules. This approach incorporates the ZPE of the solute and mitigates the clashes between the solute and solvent molecules. It has been successfully applied to surface-hopping simulations of a variety of photochemical reactions.<sup>33–37</sup>

Throughout this work, the BHLYP exchange–correlation functional<sup>38–40</sup> was employed in the hh-TDA-DFT calculations due to its superior performance in describing the excited-state properties of various organic molecules.<sup>12</sup> The TAB was first optimized on the ground state at the hh-TDA-BHLYP/6-31G\* level in the gas phase. The TAB was then solvated by either ~570 methanol or ~200 *n*-hexane molecules using the Packmol package.<sup>41</sup> MD simulations were then carried out to equilibrate the system. The system was first equilibrated in the constant NVT ensemble for ~10 ps at 300 K followed by equilibration in the constant NPT ensemble for ~10 ns at 300 K and 1 atm. A time step of 1 fs was used during the MD simulation. The cutoff for the nonbonded interactions was chosen as 10 Å. The azobenzene's coordinates were fixed throughout the simulation. The force field parameters for the azobenzene and the solvents were obtained following the general Amber force field (GAFF) procedure.<sup>42,43</sup> The point charges were derived from the restrained electrostatic potential<sup>44</sup> of TAB at the HF/6-31G\* level of theory. The resulting simulation box sizes were ~55 × 57 × 61 Å<sup>3</sup> and ~65 × 65 × 65 Å<sup>3</sup> for the TAB solvated in methanol and *n*-hexane, respectively.

The last 3 ns from the MD simulation was extracted at 100 ps intervals, resulting in 30 different snapshots. Next, I switched from periodic to free boundary conditions and reduced the system size for the QM/MM simulations in the TERACHEM package<sup>45–48</sup> (because PBCs are not yet supported in TERACHEM). For each snapshot, the TAB and any solvent molecules with at least one atom within 20 Å of the TAB's center of mass were carved out from the periodic system. The resulting spherical systems have open boundary conditions. For each trimmed snapshot, the azobenzene remained as the gas-phase equilibrium geometry due to the positional constraints during the MD simulation. Next, the TAB's configuration was replaced by a randomly sampled one from the Wigner distribution in the gas phase. The Wigner distribution was obtained using the hessian calculated at the gas-phase equilibrium geometry with the hh-TDA-BHLYP/6-31G\* method. To reduce the clashes between the solute and the solvent molecules, the solvent molecules were first optimized on the ground state using the QM/MM approach while fixing the TAB's coordinates. The QM region included the TAB molecule, while the MM region

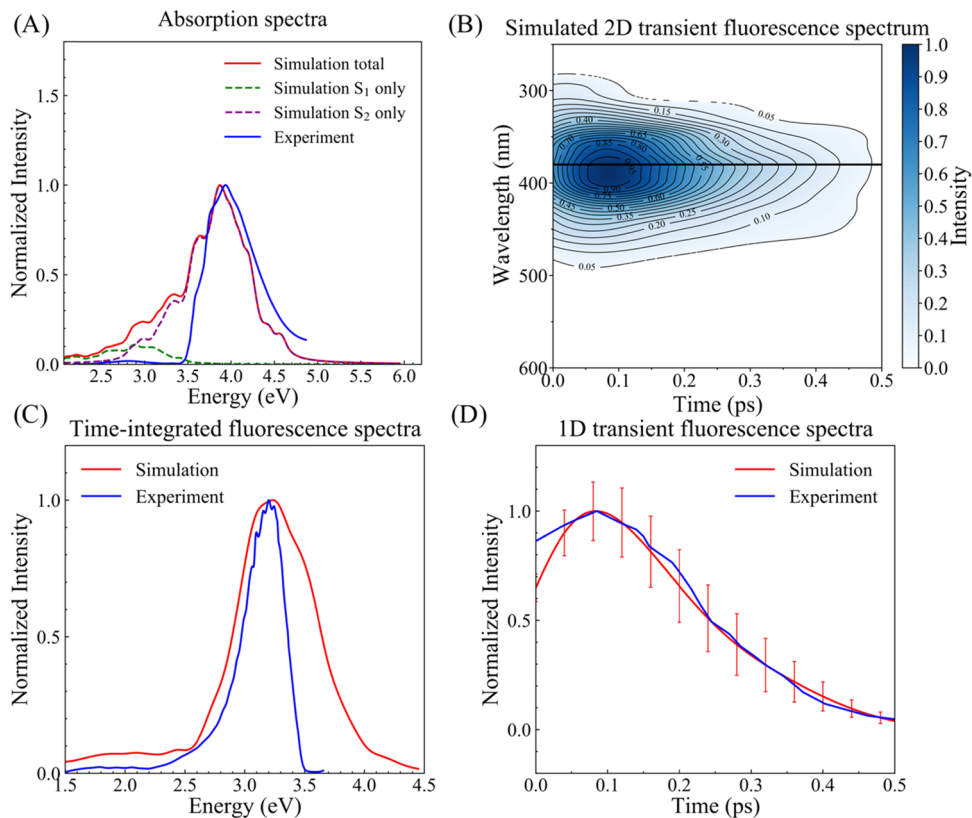


**Figure 1.** Simulated and experimental spectra<sup>56,57</sup> for the TAB's photoisomerization following the S<sub>2</sub> ( $\pi\pi^*$ ) excitation in the *n*-hexane solution are in good agreement. (A) Absorption spectra. The wavelength of maximum absorption of the simulated spectrum (red) quantitatively agrees with the experiment (blue). The green and purple dashed lines represent the contributions from the S<sub>1</sub> ( $\pi\pi^*$ ) excitation and S<sub>2</sub> excitations, respectively. (B) Simulated 2D fluorescence spectrum following the S<sub>2</sub> excitation. (C) Time-integrated fluorescence spectra. The simulated spectrum (red) is calculated by the time integration of the 2D fluorescence spectrum. The wavelength of maximum fluorescence quantitatively agrees with the experiment (blue). (D) 1D transient fluorescence spectra. The simulated spectrum (red) is extracted from the 2D fluorescence spectra at 380 nm wavelength (black horizontal line in (B)), where the experimental spectrum (blue) was probed.

included all of the solvent molecules. The QM region was treated with DFT using the BHLYP functional, while the MM region was treated with the same Amber force field as in the MD simulation. The electrostatic embedding scheme was employed to describe the electrostatic interaction between the QM and MM atoms. The electronic wavefunction of the QM atoms is solved in the presence of the electric field created by the fixed point charges of the MM atoms. In other words, the fixed point charges on the MM atoms interact with the electron density of the QM atoms. Following the QM/MM optimization, 5 ps ground-state QM/MM MD simulation was performed to further relax the solvent around the solute. Then, the ICs of the solvent molecules were taken as the positions and momenta at the last step of the QM/MM MD simulation. As described above, the ICs of the TAB solute had been sampled from the Wigner distribution to include the nuclear ZPE properly. The Wigner sampling of the TAB displaced its torsional modes around the N=N and N-C bonds from their equilibrium values, which was essential for correct description of the TAB's photodynamics. The ground-state QM/MM MD simulations were performed using TERAChem<sup>45–48</sup> interfaced with OPENMM.<sup>49</sup>

**AIMS Simulation.** The AIMS simulations started from 30 ICs for TAB solvated in both the methanol and *n*-hexane solvents and 40 ICs for TAB in the vacuum. Each AIMS simulation was run for at least 7 and 2 ps following the S<sub>1</sub> and S<sub>2</sub> excitations, respectively. The full multiple spawning (FMS)

algorithm<sup>14</sup> was employed to propagate the nuclear trajectory basis functions (TBFs) according to the time-dependent Schrödinger equation. The PES and the nonadiabatic couplings of the electronic states were calculated on-the-fly during the AIMS simulation using the QM/MM approach. The QM/MM partitioning scheme was the same as that of the ground-state MD equilibration. The QM region was treated with the hh-TDA-BHLYP/6-31G\* method with DFT-D3 dispersion correction<sup>50</sup> for all systems. The MM region was treated with the same force field as mentioned above. For the nonadiabatic dynamics simulation following the S<sub>2</sub> excitation, the Stochastic-Selection AIMS (SS-AIMS) method<sup>51</sup> was employed. The SS-AIMS method was chosen because it greatly enhances the computational efficiency with minimal loss of accuracy.<sup>51</sup> Specifically, there are frequent crossings between the S<sub>2</sub> and S<sub>1</sub> states in the initial stage of the photodynamics. According to the original AIMS algorithm, more than 20 TBFs per IC could be spawned in this scenario. Simultaneous propagation of all the TBFs would require numerous electronic structure calculations, which would significantly slow down the AIMS simulation. The SS-AIMS method<sup>51</sup> overcomes this challenge by stochastically eliminating the TBFs on-the-fly after they are decoupled. The SS-AIMS method was shown to reproduce the full AIMS simulation result after averaging over multiple reruns (usually 3–5 per IC) with different random seeds.<sup>51</sup> Three reruns of the SS-AIMS simulation were performed following the S<sub>2</sub> excitations in each system. The stochastic selection was

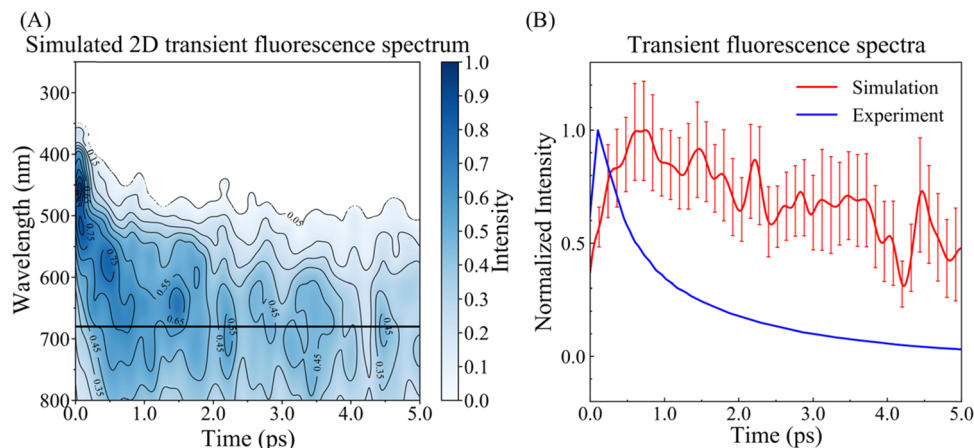


**Figure 2.** (A) Simulated 2D fluorescence spectrum following the  $S_1$  excitation. (B) 1D transient fluorescence spectra. The simulated spectrum (red) is extracted from the 2D fluorescence spectra at 680 nm wavelength (black horizontal line in (A)), where the experimental spectrum (blue) was probed.<sup>58</sup>

triggered when the maximum energy coupling between two groups of TBFs drops below  $10^{-5}$  a.u.<sup>51</sup> This energy coupling threshold corresponds to a TBF overlap threshold of  $\sim 10^{-3}$  for the systems under study. The AIMS simulations were performed using the FMS90 code interfaced with the TERAChEM/OPENMM software packages.<sup>45–49</sup>

**Absorption and Transient Fluorescence Spectral Calculations.** The absorption spectra (Figure 1A) were calculated based on a hundred ICs prepared following the same procedures mentioned above. For each IC, the  $S_0 \rightarrow S_1$  and  $S_0 \rightarrow S_2$  excitation energies and the transition dipole moments were calculated using the hh-TDA-BHLYP/Amber approach. The absorption spectrum was then calculated as described previously,<sup>52</sup> and the result was convolved in energy using a Lorentzian function with a full width at half maximum (FWHM) of 0.15 eV.

The time/energy-resolved 2D fluorescence spectrum (Figure 1B) following the  $S_2$  excitation was calculated from the AIMS simulation using eq 1:<sup>27</sup>

$$I(t, \nu) \propto \sum_{i=1,2} \sum_{I \in S_i} n_I(t) \nu^3 |\langle \Psi_{S_0}(r; \bar{R}_I(t)) | \vec{\mu} | \Psi_{S_i}(r; \bar{R}_I(t)) \rangle|^2 \quad (1)$$

where the sum is over all of the TBFs propagating on the  $S_i$  ( $i = 1, 2$ ) surface at time  $t$ ,  $n_I(t)$  is the population of the  $I$ th TBF,  $\nu = (E_{S_i}(\bar{R}_I(t)) - E_{S_0}(\bar{R}_I(t))) / h$  is the frequency,  $\vec{\mu}$  is the dipole operator,  $\Psi_{S_0/S_i}$  is the electronic wavefunction on the  $S_0/S_i$  states,  $\bar{R}_I(t)$  is the nuclear coordinate of the centroid of the  $I$ th TBF, and  $E_{S_0/S_i}(\bar{R}_I(t))$  is the potential energy on  $S_0/S_i$  states. The results were convolved in time and energy using Gaussians with FWHM of 150 fs and 0.2 eV.<sup>27</sup> The time-integrated fluorescence spectrum (Figure 1C) was calculated by integrating the 2D fluorescence spectrum over time. The 1D transient fluorescence spectrum (Figure 1D) was calculated by selecting the 1D slice from the 2D fluorescence spectrum at 380 nm, the same wavelength as the experimental probe for the stimulated emission signals.<sup>53</sup> The transient fluorescence spectra following the  $S_1$  excitation (Figure 2) were calculated using the same approach, except that the probe wavelength was set as 680 nm to be consistent with the experiment.<sup>58</sup>

**Analysis of Population Relaxation Time Constants and Quantum Yields.** To obtain the excited-state relaxation time

constants, following the  $S_1$  excitation, the time-dependent  $S_1$  population was fitted by a single exponential function (eq 2):

$$P_{S_1}(t) = \exp\left(-\frac{t}{\tau}\right) \quad (2)$$

Following the  $S_2$  excitation, the time-dependent  $S_2$  and  $S_1$  populations were fitted by eq 3, which describes the kinetics of a two-step irreversible first-order decay process:

$$\begin{aligned} P_{S_2}(t) &= \exp\left(-\frac{t}{\tau_{S_2}}\right) \\ P_{S_1}(t) &= \frac{\tau_{S_1}}{\tau_{S_1} - \tau_{S_2}} \left[ \exp\left(-\frac{t}{\tau_{S_1}}\right) - \exp\left(-\frac{t}{\tau_{S_2}}\right) \right] \end{aligned} \quad (3)$$

The error bars in the time constants were obtained by bootstrapping over 1000 random samples with replacement.

The quantum yields were calculated as follows. After the ground-state TBFs were spawned, it was propagated for 100 fs. Then, the centroids of the TBF were optimized on the ground state. The optimized geometry was assigned as the *cis* isomer if the C–N=N–C torsion's absolute value was between 0 and 15 degrees and as the *trans* isomer if it was between 165 and 195 degrees. The quantum yield was calculated as the ratio of the total population of the *cis* isomer TBFs over the total ground-state population. For SS-AIMS simulations, the quantum yields were averaged over three reruns. The error bars in the quantum yields were obtained by bootstrapping over 1000 random samples with replacement.

**Benchmark Calculation against Correlated Wavefunction Methods.** In order to further benchmark the accuracy of the hh-TDA-DFT method, the PES was characterized along the C–N=N–C ( $\theta_{\text{CNNC}}$ ) torsion of the azobenzene in the vacuum. The geometries corresponding to different  $\theta_{\text{CNNC}}$  values were obtained by constraint optimization on the  $S_0$  state using the hh-TDA-BHLYP/6-31G\*-D3 method. Then, the energies of these optimized geometries were calculated using the extended multistate complete active space second-order perturbation theory (XMS-CASPT2) method.<sup>54</sup> The XMS-CASPT2 calculations used reference wavefunctions obtained from state-averaged complete active space self-consistent field (SA-CASSCF) calculations. Following ref 23, the active space contained 10 electrons and 8 orbitals and the

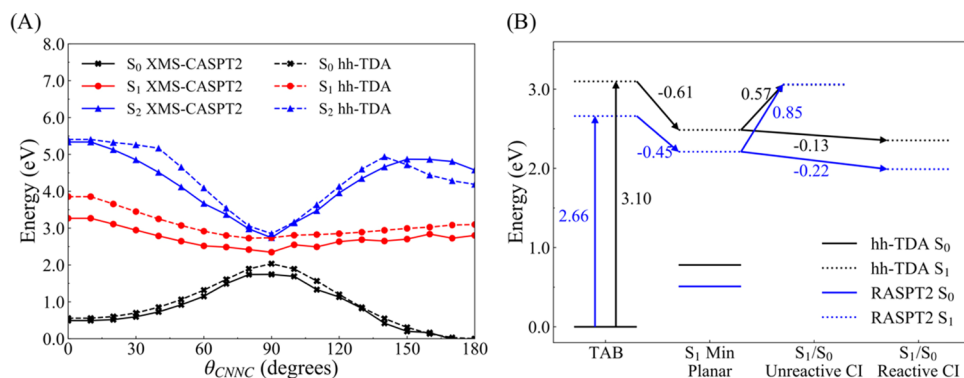


**Figure 3.** (A) Benchmark calculation of the gas-phase azobenzene's potential energy surface (PES) along the  $\theta_{\text{CNNC}}$  torsion. The S<sub>0</sub>, S<sub>1</sub>, and S<sub>2</sub> states' PES are shown in black, red, and blue, respectively. The geometry used for the energy calculations at each  $\theta_{\text{CNNC}}$  was obtained by constrained optimization on the S<sub>0</sub> state using the hh-TDA-BHLYP/6-31G\* method with DFT-D3 dispersion correction. Then, the XMS-CASPT2 energies were calculated on top of the hh-TDA-DFT-optimized geometries. The hh-TDA-DFT and XMS-CASPT2 results are shown as dashed and solid lines, respectively, and they are in parallel with each other. (B) Energies of critical points of the azobenzene in the gas phase. The hh-TDA-DFT and the RASPT2 results are shown in black and blue, respectively. For each method, the critical point geometries were first optimized before the energy calculations.<sup>22</sup> “TAB” stands for *trans* azobenzene. The RASPT2 result is obtained from ref 22.

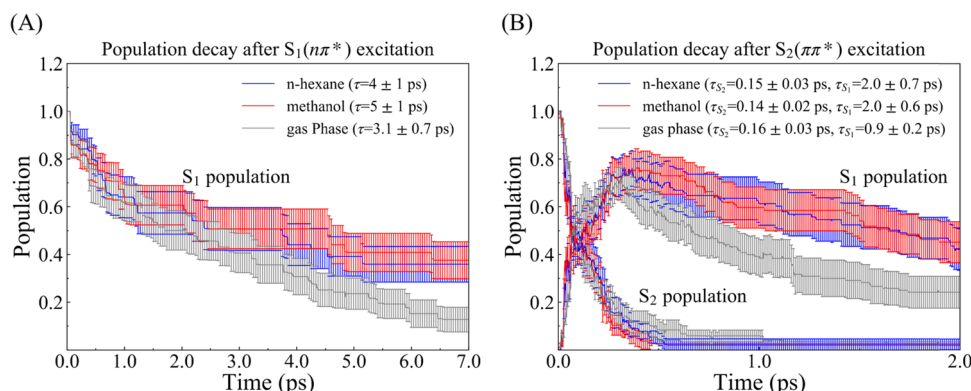


**Figure 4.** Population decay of excited states following the (A) S<sub>1</sub> and (B) S<sub>2</sub> excitations in the methanol (red) and the *n*-hexane (blue) solutions, as well as in the gas phase (gray). The population decay dynamics are similar in both solutions. The population relaxation time constants are obtained by fitting the time evolution of the excited-state populations according to the eqs 2 and 3 and are indicated in the parentheses.

state-averaging was over the three lowest singlet states (XMS-CASPT2/SA3-CASSCF(10,8)). In the XMS-CASPT2 calculations, an imaginary shift of 0.2 Hartree (with no IPEA shift) and the 6-31G\* basis set were used. The XMS-CASPT2 calculations were performed with the OPENMOLCAS package.<sup>55</sup>

In an additional benchmark calculation, the gas-phase geometries at several critical points were optimized using the hh-TDA-BHLYP/6-31G\*-D3 method. The critical points include the ground-state minimum of the *trans* isomer, the planar S<sub>1</sub> minimum, and the S<sub>1</sub>/S<sub>0</sub> reactive and unreactive conical intersections (CIs) (see the Results Section for details). The energies of these critical points were benchmarked against those previously calculated by the restricted active space second-order perturbation theory (RASPT2) method, as reported in ref 22. The RASPT2 energies were calculated with the state-averaged restricted active space self-consistent field (SA-RASSCF) reference wavefunctions. The RASSCF calculation used an active space containing 16 orbitals and 18 electrons.<sup>22</sup> The critical points were optimized by the RASPT2 method in ref 22.

## RESULTS

**Absorption and Fluorescence Spectra.** The simulated absorption and fluorescence spectra were benchmarked against

the experimental data for TAB solvated in *n*-hexane following the S<sub>1</sub> and S<sub>2</sub> excitations (Figures 1 and 2). For the S<sub>2</sub> excitation, the simulated spectra quantitatively match the wavelengths of maximum absorption and emission measured by the experiments (Figure 1A,C).<sup>56,57</sup> It is noted that in Figure 1C, the agreement between simulation and the experiment is less than perfect for large emission energies (3.4 to 4.5 eV). One possible explanation of this mismatch is that the ZPE leakage during the AIMS dynamics could make the system visit high confirms the accuracy of the hh-TDA-DF energy regions on the excited-state PES, which increases the fluorescence intensity at shorter wavelengths as compared to the experiment. Despite the mismatch at the high energy range of fluorescence signal, the general good agreement between the simulated and experimental steady-state absorption and fluorescence spectra validates the hh-TDA-DFT method's accuracy in predicting the ground-state excitation energy near the ground and the excited states' minima. Benchmark calculation of the gas-phase azobenzene's PES using the XMS-CASPT2 method<sup>54</sup> further confirms the accuracy of the hh-TDA-DFT method (Figure 3A). The adiabatic S<sub>2</sub> state's electronic wavefunction has a major π → π\* diabatic character and a minor n → π\* diabatic character, whereas the reverse is true for the adiabatic S<sub>1</sub> state. As a result, the S<sub>2</sub> state has an oscillator strength that is almost two orders of

magnitude larger than that of the  $S_1$  state.<sup>56</sup> Consequently, the  $S_0 \rightarrow S_2$  excitation dominates the absorption signal, and the  $S_2 \rightarrow S_0$  emission dominates the fluorescence signal following the  $S_2$  state excitation. It is worth noting that the transient fluorescence spectrum at 380 nm is in good agreement with the experimental spectrum measured at the same wavelength (Figure 1D). The close agreement between the simulated and experimental spectra following the  $S_2$  excitation indicates that the hh-TDA-DFT/AIMS method correctly describes the kinetics of the  $S_2$  population relaxation in the solvent environment.

Following the  $S_1$  excitation, the simulated transient fluorescence spectra are benchmarked against the experiment of Chang et al<sup>58</sup> (Figure 2). Here, the  $S_1 \rightarrow S_0$  emission dominates the fluorescence signal. At 680 nm probe wavelength, the hh-TDA-DFT/AIMS method predicts a slower decay of the fluorescence signal compared to the experiment (Figure 2B). This is a result of hh-TDA-DFT/AIMS simulation overestimating the  $S_1$  state lifetime, as discussed in detail in the next section.

**Excited-State Population Decay.** The hh-TDA-DFT/AIMS simulation quantitatively reproduced the experimental lifetimes of the  $S_2$  state but overestimated the lifetimes of the  $S_1$  state in the *n*-hexane solution<sup>56–60</sup> (Figure 4 and Table 1). A

**Table 1. Excited-State Time Constants (in Picoseconds) of the TAB Following the  $S_1$  and  $S_2$  Excitations in the *n*-Hexane Solution<sup>a</sup>**

$S_1$ excitation		$S_2$ excitation			
simulation	experiment	simulation	experiment	$\tau_{S_2}$	$\tau_{S_1}$
4 ± 1	0.1–2.5 (refs 57, 60)	$\tau_{S_2}$ 0.15 ± 0.03	$\tau_{S_1}$ 2.0 ± 0.7	$\tau_{S_2}$ 0.1–0.2 (refs 56, 57, 59)	$\tau_{S_1}$ 0.5–2.5 (refs 56, 57, 59)

<sup>a</sup>The uncertainties reported for time constants are estimated as one standard error using bootstrapping with 1000 samples.

more detailed analysis reveals that the  $S_1$  state population decays to the  $S_0$  state through two channels: a reactive one and an unreactive one. The  $S_1 \rightarrow S_0$  unreactive decay channel passes through a CI featuring a near planar geometry and two large C=N=N bending angles of ~150° (Figure 5C). The  $S_1 \rightarrow S_0$  reactive decay channel passes through a CI featuring a twisted C=N=N-C torsion of ~90° (Figure 5F). The difference in the two CIs' geometry leads to different outcomes following the decay through the two channels. All of the  $S_0$  state TBFs that are spawned through the unreactive CI end up as the *trans* isomer, while the ones spawned through the reactive CI have a ~30–50% chance to end up as the *cis* isomer (Figure 5A,B,D,E). As has been discovered in previous studies, the reactive and unreactive  $S_1/S_0$  CIs belong to the same crossing seam.<sup>16,17,22</sup>

The  $S_1 \rightarrow S_0$  decay through the two channels is separated in time, and the unreactive decay occurs earlier than the reactive decay (Table 2). The decay through the reactive channel is slow because the C=N=N-C torsion needs to rotate from ~180 to ~90° to access the  $S_1/S_0$  reactive CI (Figure 5F). In this process, the two phenyl rings that are initially co-planar in the TAB need to reorient themselves. In agreement with the findings of previous studies,<sup>17,20</sup> the concerted motion of the N atoms and rotation of the N-C bonds avoid displacing the phenyl rings too much. In this process, the solvent molecules need to be reorganized in order to accommodate the structural change of the solute. The necessary rearrangement of the solvent molecules is limited by their diffusion rate, which postpones

the access to the  $S_1/S_0$  reactive CI. In contrast, the  $S_1/S_0$  unreactive CI can be readily accessed by symmetrical bending of the two C=N=N angles near 150°, without significant twisting of the C=N=N-C torsion (Figure 5C). Even though the  $S_1/S_0$  unreactive CI has a higher energy than the reactive CI (0.70 eV difference in the gas phase, Figure 3B), the energy from the photoexcitation combined with the ZPE provides sufficient energy to power the bending of the two C=N=N angles, giving rise to the initial  $S_1 \rightarrow S_0$  unreactive decay within 400 fs (Table 2). However, the kinetic energy of the solute is quickly dissipated to the solvent molecules, and the unreactive decay channel becomes gradually inaccessible. After one picosecond, only the  $S_1 \rightarrow S_0$  reactive decay channel remains accessible.

The excitation wavelength also affects the population decay dynamics. The decay of the  $S_1$  state population is faster following the  $S_2$  excitation than following the  $S_1$  excitation (Figure 4). This is because following the  $S_2$  excitation, the  $S_2 \rightarrow S_1$  decay provides extra kinetic energy for the azobenzene to quickly access the  $S_1/S_0$  reactive CI compared to the case of  $S_1$  excitation. As shown in Table 2, the average time it takes to access the  $S_1/S_0$  reactive CI following the  $S_2$  excitation is ~60–70% of the one following the  $S_1$  excitation.

The solvent environment slows down the  $S_1 \rightarrow S_0$  reactive decay compared to gas-phase dynamics (Table 2). The delayed access to the  $S_1/S_0$  reactive CI indicates that the solvent molecules hinder the central C=N=N-C torsional motion of the azobenzene on the excited state. Interestingly, despite the large difference in the dielectric constants between the *n*-hexane ( $\epsilon \sim 2$ ) and the methanol ( $\epsilon \sim 33$ ), the two solvents slow down the twisting of the TAB to a similar extent. Therefore, the solvent's effect on the photodynamics is not very sensitive to its polarity. Interestingly, the methanol molecules rarely form hydrogen bonds with the azobenzene on the  $S_1$  state. Transient hydrogen bonds between the azobenzene and the methanol are only formed in 5 out of the 30 ICs following the  $S_1$  excitation. The transient hydrogen bonds are only formed when the azobenzene is about to access the  $S_1/S_0$  reactive CI. Due to partial rotation of the C=N=N-C bond, the two nitrogen atoms are more exposed to the solvent to receive the hydrogen bonds donated by the methanol's hydroxyl groups.

To understand why the hh-TDA-DFT/AIMS method overestimates the  $S_1$  state lifetime, the energies of critical geometries of gas-phase azobenzene are benchmarked against the RASPT2 energies reported in ref 22 (Figure 3B). The hh-TDA-BHLYP/6-31G\*-D3 method predicts a 0.13 eV energy difference between the  $S_1$  planar minimum and the  $S_1/S_0$  reactive CI and a 0.1 eV torsional barrier going from the former to the latter. The RASPT2 method predicts a 0.22 eV energy difference between the  $S_1$  planar minimum and the  $S_1/S_0$  reactive CI and almost no torsional barrier going from the former to the latter. This suggests that the hh-TDA-DFT method overestimates the CNNC torsion's rotational energy barrier on the  $S_1$  state, leading to a slower  $S_1 \rightarrow S_0$  decay through the reactive channel.

Although there are discrepancies between the simulated and experimental fluorescence spectra following the  $S_1$  excitation and between the hh-TDA-DFT and RASPT2 energies at critical points, such discrepancies do not necessarily suggest that the hh-TDA-DFT method is qualitatively incorrect. A number of experimental studies have confirmed the existence of a picosecond component of the  $S_1$  state lifetime.<sup>57–63</sup> In a recent experiment using a jet-cooled molecular beam and multiphoton ionization technique,<sup>63</sup> the  $S_1$  state barrier and lifetime were

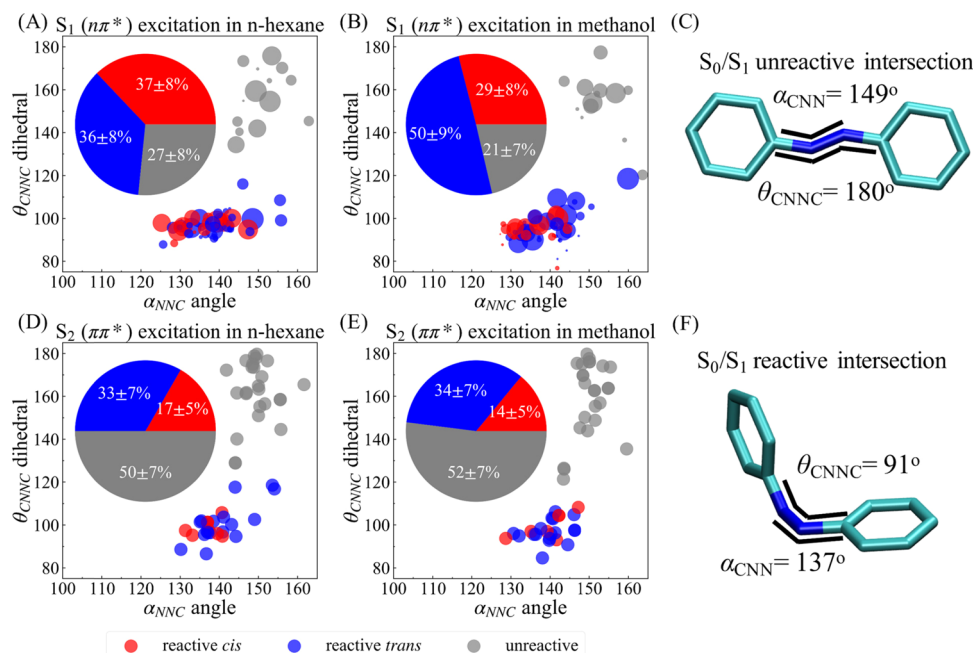


**Figure 5.** In the *n*-hexane and methanol solutions, the  $S_2$  excitation leads to a smaller isomerization quantum yield than the  $S_1$  excitation due to more  $S_1 \rightarrow S_0$  unreactive decay. (A, B, D, E) Decomposition of the  $S_1 \rightarrow S_0$  population decay following the  $S_1$  or  $S_2$  excitation in the two solvents. Each circle represents a  $S_0$  state TBF. Its location is determined by the geometry at the centroid of the TBF at its spawning time, i.e., the larger one of the two  $C-N=N$  angles ( $\alpha_{CNN}$ ) and the  $C-N=N-C$  torsion ( $\theta_{CNNC}$ ). The circles' coloring scheme categorizes the origins and fates of the  $S_0$  state TBFs into three classes. The circle is gray if the TBF is spawned through an  $S_1/S_0$  unreactive CI (shown in C). By definition, this type of TBF ends up as the *trans* isomer. The circle is red (or blue) if the TBF is spawned through an  $S_1/S_0$  reactive CI (shown in F) and ends up as the *cis* (or *trans*) isomer. The area of each circle represents the eventual amplitude of the  $S_0$  state TBFs. The  $S_2$  excitation dynamics are performed with the SS-AIMS method (see the “Methods Section”). After the stochastic selection, there is only one  $S_0$  TBF left for each IC in each rerun. Thus, the eventual population of each  $S_0$  TBF is equal to one. The pie charts in the insets indicate the relative populations of the  $S_0$  state TBFs in each of the three categories. The uncertainties are estimated as one standard error using bootstrapping with 1000 samples.

**Table 2. Average Timepoints (in Picoseconds) of the  $S_1 \rightarrow S_0$  Spawning Events for Each Class of Decay Pathways<sup>a</sup>**

pathway	average timepoint of spawning events		
	<i>n</i> -hexane	methanol	vacuum
$S_1/S_0$ reactive ( $S_1$ excitation)	$1.9 \pm 0.2$	$2.2 \pm 0.3$	$1.0 \pm 0.1$
$S_1/S_0$ unreactive ( $S_1$ excitation)	$0.4 \pm 0.1$	$0.19 \pm 0.06$	$0.4 \pm 0.1$
$S_2/S_1$ planar $\rightarrow S_1/S_0$ reactive ( $S_2$ excitation)	$1.2 \pm 0.1$	$1.2 \pm 0.1$	$0.74 \pm 0.05$
$S_2/S_1$ planar $\rightarrow S_1/S_0$ unreactive ( $S_2$ excitation)	$0.39 \pm 0.06$	$0.35 \pm 0.08$	$0.53 \pm 0.08$
$S_2/S_1$ twisted $\rightarrow S_1/S_0$ reactive ( $S_2$ excitation)	$0.43 \pm 0.03$	$0.40 \pm 0.02$	NA

<sup>a</sup>The pathways are categorized by the types of  $S_1/S_0$  (reactive or unreactive) and  $S_2/S_1$  (planar or twisted) CIs, following the  $S_1$  and  $S_2$  excitations in the *n*-hexane and methanol solutions. The uncertainties reported for the average timepoints are estimated as one standard error using bootstrapping with 1000 samples.

measured to be  $\sim 2$  kcal/mol and 13 ps at low rotational temperature, respectively. The barrier is in good agreement with the hh-TDA-DFT calculation (Figure 3B). A previous Raman spectral measurement<sup>59</sup> determined the  $S_1$  lifetime to be  $\sim 1$  ps in *n*-hexane. Several transient absorption spectral measurements<sup>57,60–62</sup> determined that the  $S_1$  relaxation dynamics have a slow component of  $\sim 2\text{--}3$  ps. In the transient fluorescence measurement by Chang et al.,<sup>58</sup> the  $S_1$  relaxation dynamics have a component of  $\sim 1.7\text{--}2.0$  ps at 680 nm probe wavelength with an amplitude ranging from 0.41 to 0.49. At shorter probe wavelengths, the amplitude is smaller but still beyond 0.24.

Chang et al.<sup>58</sup> attributed this picosecond timescale component to the torsional dynamics of the azobenzene. Therefore, the hh-TDA-DFT/AIMS method is able to quantitatively describe the  $S_2 \rightarrow S_1$  population relaxation dynamics following the  $S_2$  excitation and qualitatively describe the picosecond torsional dynamics of azobenzene on the  $S_1$  state.

The slower torsional dynamics on the  $S_1$  state as predicted by the hh-TDA-DFT method can be partly attributed to the neglect of solvent ZPE in addition to the overestimation of the  $S_1$  state torsion barrier. Including the solvent ZPEs in the ICs would facilitate the  $S_1 \rightarrow S_0$  decay through the reactive channel because the solvent molecules could diffuse and reorganize themselves faster. However, this is a challenging task due to the presence of the soft vibrational modes in the bulk solvent molecules, so it was not implemented in the current work. It will be exciting to test such hypothesis in future simulations.

The ICs of the solute molecule include ZPE through Wigner sampling, and they have higher energies than the ICs sampled from Boltzmann distribution. The inclusion of more energy in the ICs could affect the kinetics of the photoisomerization reaction. Indeed, as shown in Table S1, following the  $S_1$  excitation of TAB in the vacuum, a higher initial energy leads to a faster decay of the  $S_1$  state population. However, the excited-state lifetimes following the  $S_2$  excitation do not sensitively depend on the amount of initial energy in the system. Obviously, the problem of ZPE leakage is present in the classical dynamics of the nuclei during the AIMS simulation. In particular, since the TBFs move classically, each vibrational mode  $i$  is not obliged to keep the  $\frac{1}{2}\hbar\omega_i$  ZPE locked to itself. The solute molecule can

exploit the ZPE to reach points of the phase space that would be hardly accessible quantum mechanically. The ZPE leakage could facilitate the  $S_1 \rightarrow S_0$  decay through both the unreactive and reactive  $S_1/S_0$  CIs, so it is difficult to predict its overall effect on the branching ratio between these two decay channels. However, the presence of ZPE in a realistic molecular system is undeniable. Thus, only including the classical energy in the ICs cannot faithfully represent the dynamics and energetics of the realistic system, unless the ZPE has been implicitly taken into account in the construction of PES. It is well known that the exclusion of ZPE in ab initio MD simulation can slow down barrier crossing reactions and the diffusion of the molecules, which is a main source of deviation from the experimental data.<sup>64,65</sup> In the hh-TDA-DFT/AIMS simulations, the ZPE was not taken into account in the ab initio PES. Therefore, in my opinion, it is necessary to include the ZPE in the ICs to account for the nuclear quantum effect despite the presence of the ZPE leakage. Indeed, the IC preparation procedure has been successfully applied in a number of surface-hopping simulation studies by Lischka et al.<sup>33–37</sup> Moreover, the Wigner sampling of the ICs has been frequently employed to prepare ICs for the AIMS simulations.<sup>13</sup>

**Wavelength-Dependent Quantum Yields.** One of the fascinating aspects of azobenzene photodynamics is the wavelength dependence of its isomerization quantum yield. The experimentally measured quantum yield following the  $S_1$  and  $S_2$  excitations ranges from 0.2–0.3 and 0.1–0.15, respectively<sup>4–9</sup> (Table 3). The simulation correctly predicts

**Table 3. Quantum Yields of the TAB's Photoisomerization in the *n*-Hexane and Methanol Solutions and in the Vacuum, Following the  $S_1$  and  $S_2$  Excitations<sup>a</sup>**

system	$S_1$ excitation		$S_2$ excitation	
	simulation	experiment	simulation	experiment
<i>n</i> -hexane	0.37 ± 0.08	0.25 (ref 5)	0.16 ± 0.05	0.11 (ref 5)
methanol	0.29 ± 0.08	0.22–0.31 (refs 7, 9)	0.14 ± 0.05	0.12–0.15 (refs 7, 9)
vacuum	0.28 ± 0.06	NA	0.16 ± 0.04	NA

<sup>a</sup>The uncertainties reported for quantum yields are estimated as one standard error using bootstrapping with 1000 samples.

the wavelength dependence of the quantum yield in both solutions compared with experimental data (Table 3). To analyze the cause of the wavelength-dependent quantum yield, we categorize each  $S_0$  state TBF according to the type of the  $S_1/S_0$  CI through which it was spawned (Figure 5). Based on this analysis, it is evident that the lower quantum yield following the  $S_2$  excitation is due to the increased access to the  $S_1 \rightarrow S_0$  unreactive decay channel by symmetric bending of the two  $C=N=N$  angles. Following the  $S_2$  excitation, the  $S_0$  state TBFs spawned through the  $S_1/S_0$  unreactive CI account for ~50% of the  $S_0$  state population. In contrast, following the  $S_1$  excitation, the same type of TBF accounts for less than 30% of the  $S_0$  state population. Because these TBFs exclusively end up as the *trans* isomer, their population's difference largely contributes to the wavelength dependence of the isomerization quantum yield.

The difference in the accessibility of the  $S_1 \rightarrow S_0$  unreactive decay channel following the  $S_1$  and  $S_2$  excitations can be explained from an energetic perspective. In the gas phase, the  $S_1/S_0$  unreactive CI is 0.57 eV higher in energy than the  $S_1$  state planar minimum geometry (Figure 3B). In the solvent, the TAB

also needs to overcome a large energy barrier to access this CI. Following the  $S_2$  excitation, the  $S_2$  state population decays quickly to the  $S_1$  state within 200 fs (Table 1 and Figure 4). The decay is dominantly through a  $S_2/S_1$  planar CI featuring a  $C=N=N-C$  torsion of ~180° and two  $C-N=N$  angles of ~108° (Figure 6C). Therefore, right after the  $S_2 \rightarrow S_1$  transition, the

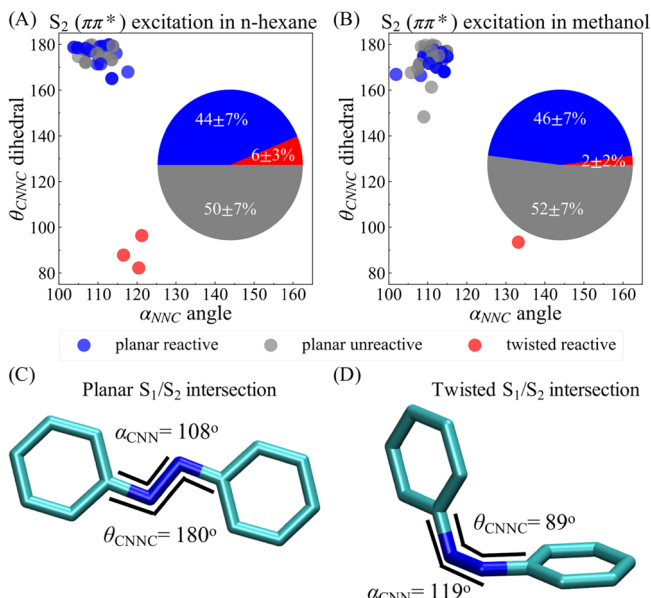


**Figure 6.** Following the  $S_2$  excitation, most of the  $S_2$  state population decays to the  $S_1$  state through the  $S_2/S_1$  planar CI, about half of which further decays to  $S_0$  state through the  $S_1/S_0$  unreactive CI. (A–B) Decomposition of the  $S_2 \rightarrow S_1$  population decay following the  $S_2$  excitation in the *n*-hexane and methanol solutions. Each circle represents a  $S_1$  state TBF. The circle's location is determined by the geometric feature ( $\theta_{CNNC}$  and  $\alpha_{CNN}$ ) of the TBF's centroid at the spawning event. The circles' coloring scheme categorizes the origins and fates of the  $S_1$  state TBFs into three classes. The circle is gray (or blue) if the TBF is spawned through the  $S_2/S_1$  planar CI (shown in C) and further decays to the  $S_0$  state through the  $S_1/S_0$  unreactive (or reactive) CI, respectively. The circle is red if the TBF is spawned through an  $S_2/S_1$  twisted CI (shown in D) and inevitably further decays to the  $S_0$  state through the  $S_1/S_0$  reactive CI. Each circle's area represents the eventual population of the  $S_1$  state TBF before it spawns any TBFs on the  $S_0$  state. The pie charts in the insets indicate the relative populations of the  $S_1$  state TBFs in each of the three categories.

value of the  $C=N=N$  angle is far smaller than that of the  $S_1$  state planar minimum geometry (~129°). The excess potential energy in this angle bending mode translates quickly to the kinetic energy, which enlarges the two angles symmetrically to access the  $S_1/S_0$  unreactive CI (Figure 5C). The system decays to the  $S_0$  state through this CI with a  $C=N=N-C$  torsion beyond 120° (Figure 5D,E). However, the kinetic energy is insufficient to overcome the ground-state torsional barrier (more than 0.8 eV) in order for the azobenzene to end up as the *cis* isomer (Figure 3A). As a result, the  $S_1 \rightarrow S_0$  unreactive decay channel exclusively leads to the *trans* isomer. On the other hand, the total energy of the system is less following the  $S_1$  excitation, so there is less kinetic energy available to access the  $S_1/S_0$  unreactive CI. As a result, a much lower percentage of TBFs is able to decay through the  $S_1 \rightarrow S_0$  unreactive channel compared to following the  $S_2$  excitation. Interestingly, if the type of excitation (either  $S_1$  or  $S_2$ ) is the same, then the quantum yields are not sensitive to the initial energy of the ICs (Table S2). This

is probably because the variation in the energy of the ICs is not as significant as the difference between the  $S_0 \rightarrow S_1$  vs  $S_0 \rightarrow S_2$  excitation energies.

In comparison with the RASPT2 method, the hh-TDA-DFT method underestimates the energy gap between the reactive and unreactive  $S_1/S_0$  CIs. The RASPT2/hh-TDA-DFT method predicts that the  $S_1/S_0$  unreactive CI is 1.07/0.70 eV higher in energy than the  $S_1/S_0$  reactive CI. Thus, the hh-TDA-DFT method underestimates the energy gap between the two CIs compared to the RASPT2 method. This suggests that the hh-TDA-DFT/AIMS simulation could overestimate the population decay through the  $S_1/S_0$  unreactive CI. However, this hypothesis needs to be verified in the future by direct comparison with the RASPT2/AIMS simulations.

In addition, for the  $S_0$  state TBFs spawned through the  $S_1/S_0$  reactive CI, the direction of the C–N=N–C torsion's velocity at the spawning time largely determines the final isomer of the azobenzene. As shown in Figure 7, when the direction of the torsional velocity is toward forming the *cis* isomer, the spawned TBF will most likely end up in the *cis* isomer minimum. In contrast, the opposite direction of the torsional velocity will certainly lead to the *trans* isomer minimum. This phenomenon is observed in both solvent systems (Figure 7). Interestingly, the

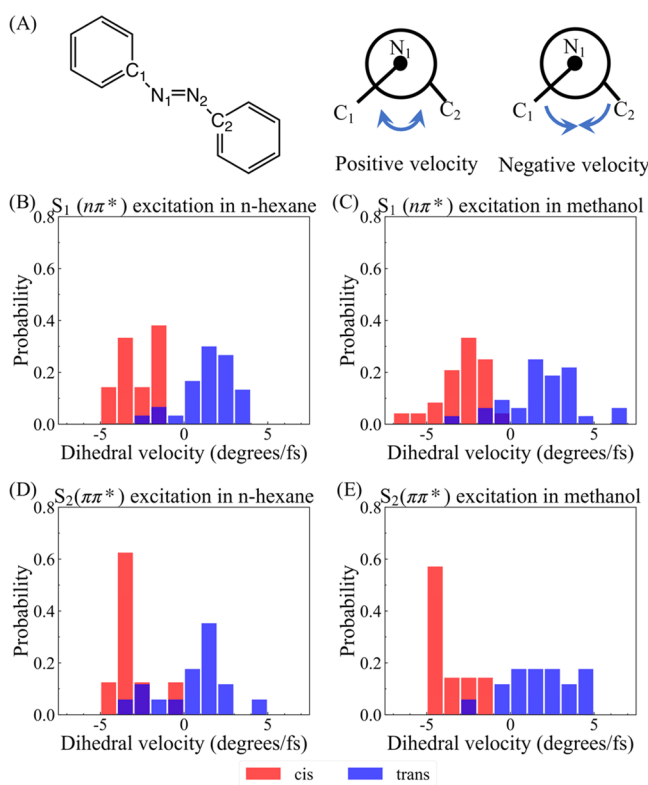


**Figure 7.** C–N=N–C torsional motion's directionality at the  $S_1 \rightarrow S_0$  spawning time largely determines the final isomer in the *n*-hexane and methanol solutions. (A) Definitions of the signs of the dihedral velocity. The four atoms in the dihedral are labeled on the chemical structure. The signs of dihedral velocity are defined on the Newman projections, and the arrows represent the torsional motion at the reactive CI. (B–E) Probability of generating the *cis* and *trans* isomers as a function of dihedral velocity at the spawning time. The x axis indicates the dihedral velocities of the centroids of the TBFs at the spawning time, and the y axis indicates the probabilities corresponding to the torsional velocities in the histogram. The bars are labeled as red or blue if the  $S_0$  state TBF ends up as the *cis* or *trans* isomer, respectively.

dynamics of the hydrogen-out-of-plan mode of the retinal protonated Schiff base were also essential in determining the chromophore's quantum yield in rhodopsins.<sup>66–68</sup> It is worth noting that the directionality of the C–N=N–C torsion only affects the final isomer for the  $S_1 \rightarrow S_0$  decay through the reactive CI. For the decay through the unreactive CI, the directionality of the C–N=N–C torsion does not matter much and the spawned TBFs will all end up as the *trans* isomer. Moreover, the  $S_2$  excitation also leads to a less branching ratio for the *cis* isomer through the  $S_1 \rightarrow S_0$  reactive decay channel as compared to the case following  $S_1$  excitation, which also partly contributes to the higher quantum yield following the  $S_1$  excitation.

The TBFs remaining on the excited state at the end of the AIMS simulation account for 30–40% of the total population (Figure 4). In principle, all of the excited-state TBFs need to decay to the ground state before the quantum yield can be evaluated. In practice, due to the slow dynamics on the  $S_1$  state (see the “Excited-State Population Decay” Section) and the necessity of multiple reruns in SS-AIMS simulation, doing so would cost a significant amount of computer resource without qualitatively changing the conclusion. The quantum yield was found to change minimally after 5/1.5 ps following the  $S_1$  and  $S_2$  excitations, respectively. Therefore, as an approximation, only the ground-state TBFs at the end of the AIMS simulation were used to calculate the quantum yield. Further extending the simulation to deplete all excited-state TBFs could slightly increase the quantum yield by 0.05–0.07 for both the  $S_1$  and  $S_2$  excitations. As a result, the quantum yields could be slightly overestimated compared to the experiment, but the wavelength dependence of the quantum yield would still be present. Such an estimation is based on the branching ratio at the  $S_1/S_0$  reactive CI (Figure 5A,B,D,E), which is the only energetically accessible  $S_1 \rightarrow S_0$  decay channel beyond the picosecond time regime.

As a qualitative illustration of the azobenzene's photodynamics through different decay channels, Figure 8 depicts the evolution of a typical  $S_1$  state TBF following the  $S_2$  excitation in the methanol solution. The two C–N=N angle bending

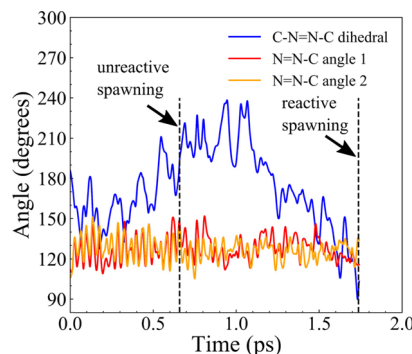


**Figure 8.** A  $S_1$  state TBF evolves to access the  $S_1/S_0$  unreactive and reactive CIs, triggering two spawning events. The  $S_1$  state TBF is extracted from the AIMS simulation following the  $S_2$  excitation in the methanol solution. The  $S_1$  state TBF is initially spawned from its parent TBF on the  $S_2$  state. The timepoint of this event defines the origin on the x axis. The dashed lines and arrows indicate the spawning events through the  $S_1/S_0$  reactive and unreactive CIs. The blue line indicates the evolution of the C–N=N–C torsion, and the red and orange lines indicate the evolution of the two C–N=N angles. The unreactive spawning occurs at a large C–N=N bending angle ( $\sim 148^\circ$ ) and near planar C–N=N–C torsion ( $\sim 193^\circ$ ). The reactive spawning event occurs at a smaller C–N=N bending angle ( $\sim 135^\circ$ ) and near perpendicular C–N=N–C torsion ( $\sim 95^\circ$ ).

modes and the central C=N=N-C dihedral rotational mode are plotted as a function of time. The time zero is set at the S<sub>2</sub>→S<sub>1</sub> spawning event, which creates the S<sub>1</sub> state TBF. The values of the two angles initially oscillate with large amplitudes following the S<sub>2</sub>→S<sub>1</sub> decay due to high kinetic energy. When the angles oscillate close to 150°, e.g., at  $t = \sim 0.67$  ps, the S<sub>1</sub> state TBF reaches an S<sub>1</sub>/S<sub>0</sub> unreactive CI through which one S<sub>0</sub> state TBF is spawned. The centroid of this TBF eventually ends up as the *trans* isomer. Later on, the oscillations of the two angle bending modes are gradually damped by energy dissipation to the solvent. As a result, the S<sub>1</sub>/S<sub>0</sub> unreactive CI can no longer be accessed by the symmetrical angle bending after 1 picosecond. The rotation of the C=N=N-C torsion takes place at a longer time than the bending of the C-N=N angles. At  $t = \sim 1.72$  ps, the C=N=N-C torsion crosses the energy barrier and becomes nearly 90 degrees, reaching the S<sub>1</sub>/S<sub>0</sub> reactive CI. Then, another S<sub>0</sub> state TBF is spawned. However, this TBF eventually ends up as the *trans* isomer because the dihedral velocity at S<sub>1</sub>→S<sub>0</sub> spawning timepoint is toward forming the *trans* isomer.

Overall, the above findings point to critical dynamical effects in the isomerization quantum yield of the azobenzene. The C=N=N-C torsional mode and the C-N=N angle bending modes are essential factors that affect the formation of the photoproduct.

## CONCLUSIONS

In this work, the first-principles nonadiabatic dynamics simulations of TAB's photodynamics were performed for the first time in two explicit solvents: *n*-hexane and methanol. The “on-the-fly” electronic structure calculations during the non-adiabatic dynamics simulation include both the static and dynamic electron correlations. The calculated spectra are in near quantitative agreement with experiments following the S<sub>2</sub> excitation.<sup>56,57,59</sup> The simulation overestimates the fluorescence lifetime following the S<sub>1</sub> excitation, possibly due to a slight overestimation of the S<sub>1</sub> state's torsional barrier<sup>22</sup> and the neglect of the ZPE of solvent molecules. Nonetheless, the simulation is able to qualitatively reproduce the picosecond timescale of the torsional dynamics on the S<sub>1</sub> state measured by the experiments.<sup>57–63</sup> The photodynamics exhibit a noticeable solvation effect. The solvent molecules slow down the photoisomerization of the *trans* azobenzene by slowing down the S<sub>1</sub>→S<sub>0</sub> reactive decay. Also, the wavelength dependence of isomerization quantum yield is conserved in both types of solvents. The S<sub>2</sub> excitation allows easier access to the S<sub>1</sub>→S<sub>0</sub> uncreative decay channel than the S<sub>1</sub> excitation, resulting in a lower quantum yield. The dynamics of the central torsion and angles of azobenzene play a critical role in determining the eventual photoproduct of the reaction. This benchmark study lays the foundation for future simulations of azobenzene-derived molecular photoswitches in photoactive biological and material systems.

## ASSOCIATED CONTENT

### Supporting Information

The Supporting Information is available free of charge at <https://pubs.acs.org/doi/10.1021/acs.jctc.1c00105>.

(Tables S1 and S2) Dependence of excited-state lifetimes and quantum yields on the total energy of the initial conditions ([PDF](#))

## AUTHOR INFORMATION

### Corresponding Author

Ruibin Liang – Department of Chemistry and Biochemistry, Texas Tech University, Lubbock, Texas 79409, United States;  
Email: [rliang@ttu.edu](mailto:rliang@ttu.edu)

Complete contact information is available at:  
<https://pubs.acs.org/10.1021/acs.jctc.1c00105>

### Notes

The author declares no competing financial interest.

## ACKNOWLEDGMENTS

This work was supported by the startup funds from Texas Tech University. The researcher used GPU computing facilities provided by the High Performance Computing Center at Texas Tech University as well as the Innovation Lab from Dell Inc. The researcher is grateful for the helpful discussions with Prof. Todd J. Martínez, Dr. Jimmy K. Yu, and Dr. Christoph Bannwarth at Stanford University.

## REFERENCES

- (1) Szymański, W.; Beierle, J. M.; Kistemaker, H. A. V.; Velema, W. A.; Feringa, B. L. Reversible Photocontrol of Biological Systems by the Incorporation of Molecular Photoswitches. *Chem. Rev.* **2013**, *113*, 6114–6178.
- (2) Pianowski, Z. L. Recent Implementations of Molecular Photoswitches into Smart Materials and Biological Systems. *Chem. – Eur. J.* **2019**, *25*, 5128–5144.
- (3) Pathem, B. K.; Claridge, S. A.; Zheng, Y. B.; Weiss, P. S. Molecular Switches and Motors on Surfaces. *Annu. Rev. Phys. Chem.* **2013**, *64*, 605–630.
- (4) Rau, H. Further evidence for rotation in the  $\pi,\pi^*$  and inversion in the  $n,\pi^*$  photoisomerization of azobenzenes. *J. Photochem. Photobiol. A* **1984**, *26*, 221–225.
- (5) Bortolus, P.; Monti, S. Cis-trans photoisomerization of azobenzene. Solvent and triplet donors effects. *J. Phys. Chem.* **1979**, *83*, 648–652.
- (6) Bortolus, P.; Monti, S. cis  $\rightleftharpoons$  trans Photoisomerization of azobenzene-cyclodextrin inclusion complexes. *J. Phys. Chem.* **1987**, *91*, 5046–5050.
- (7) Ladányi, V.; Dvořák, P.; Al Anshori, J.; Vetráková, L'; Wirz, J.; Heger, D. Azobenzene photoisomerization quantum yields in methanol redetermined. *Photochem. Photobiol. Sci.* **2017**, *16*, 1757–1761.
- (8) Gauglitz, G.; Hubig, S. Chemical actinometry in the UV by azobenzene in concentrated solution: A convenient method. *J. Photochem. Photobiol. A* **1985**, *30*, 121–125.
- (9) Ronayette, J.; Arnaud, R.; Lebourgeois, P.; Lemaire, J. Isomérisation photochimique de l'azobenzène en solution. I. *Can. J. Chem.* **1974**, *52*, 1848–1857.
- (10) Yu, J. K.; Bannwarth, C.; Liang, R.; Hohenstein, E. G.; Martínez, T. J. Nonadiabatic Dynamics Simulation of the Wavelength-Dependent Photochemistry of Azobenzene Excited to the  $n\pi^*$  and  $\pi\pi^*$  Excited States. *J. Am. Chem. Soc.* **2020**, *142*, 20680–20690.
- (11) Bannwarth, C.; Yu, J. K.; Hohenstein, E. G.; Martínez, T. J. Hole–hole Tamm–Dancoff-approximated density functional theory: A highly efficient electronic structure method incorporating dynamic and static correlation. *J. Chem. Phys.* **2020**, *153*, 024110.
- (12) Yu, J. K.; Bannwarth, C.; Hohenstein, E. G.; Martínez, T. J. Ab Initio Nonadiabatic Molecular Dynamics with Hole–Hole Tamm–Dancoff Approximated Density Functional Theory. *J. Chem. Theory Comput.* **2020**, *16*, 5499–5511.
- (13) Curchod, B. F. E.; Martínez, T. J. Ab Initio Nonadiabatic Quantum Molecular Dynamics. *Chem. Rev.* **2018**, *118*, 3305–3336.
- (14) Ben-Nun, M.; Quenneville, J.; Martínez, T. J. Ab Initio Multiple Spawning: Photochemistry from First Principles Quantum Molecular Dynamics. *J. Phys. Chem. A* **2000**, *104*, 5161–5175.

- (15) Ben-Nun, M.; Martínez, T. J. Ab Initio Quantum Molecular Dynamics. In *Adv. Chem. Phys.*; Prigogine, I.; Rice, S. A. Eds.; John Wiley & Sons, Inc., 2002; 121, 439–512.
- (16) Ciminelli, C.; Granucci, G.; Persico, M. The Photoisomerization Mechanism of Azobenzene: A Semiclassical Simulation of Nonadiabatic Dynamics. *Chem. – Eur. J.* **2004**, 10, 2327–2341.
- (17) Granucci, G.; Persico, M. Excited state dynamics with the direct trajectory surface hopping method: azobenzene and its derivatives as a case study. *Theor. Chem. Acc.* **2007**, 117, 1131–1143.
- (18) Xu, C.; Yu, L.; Gu, F. L.; Zhu, C. Probing the  $\pi \rightarrow \pi^*$  photoisomerization mechanism of trans-azobenzene by multi-state ab initio on-the-fly trajectory dynamics simulations. *Phys. Chem. Chem. Phys.* **2018**, 20, 23885–23897.
- (19) Toniolo, A.; Ciminelli, C.; Persico, M.; Martínez, T. J. Simulation of the photodynamics of azobenzene on its first excited state: Comparison of full multiple spawning and surface hopping treatments. *J. Chem. Phys.* **2005**, 123, 234308.
- (20) Cusati, T.; Granucci, G.; Persico, M. Photodynamics and Time-Resolved Fluorescence of Azobenzene in Solution: A Mixed Quantum-Classical Simulation. *J. Am. Chem. Soc.* **2011**, 133, 5109–5123.
- (21) Cantatore, V.; Granucci, G.; Persico, M. Simulation of the  $\pi \rightarrow \pi^*$  photodynamics of azobenzene: Decoherence and solvent effects. *Comput. Theor. Chem.* **2014**, 1040–1041, 126–135.
- (22) Aleotti, F.; Soprani, L.; Nenov, A.; Berardi, R.; Arcioni, A.; Zannoni, C.; Garavelli, M. Multidimensional Potential Energy Surfaces Resolved at the RASPT2 Level for Accurate Photoinduced Isomerization Dynamics of Azobenzene. *J. Chem. Theory Comput.* **2019**, 15, 6813–6823.
- (23) Casellas, J.; Bearpark, M. J.; Reguero, M. Excited-State Decay in the Photoisomerisation of Azobenzene: A New Balance between Mechanisms. *ChemPhysChem* **2016**, 17, 3068–3079.
- (24) Cembran, A.; Bernardi, F.; Garavelli, M.; Gagliardi, L.; Orlandi, G. On the Mechanism of the cis–trans Isomerization in the Lowest Electronic States of Azobenzene: S0, S1, and T1. *J. Am. Chem. Soc.* **2004**, 126, 3234–3243.
- (25) Minezawa, N.; Gordon, M. S. Photoisomerization of Stilbene: A Spin-Flip Density Functional Theory Approach. *J. Phys. Chem. A* **2011**, 115, 7901–7911.
- (26) Nenov, A.; Borrego-Varillas, R.; Oriana, A.; Ganzer, L.; Segatta, F.; Conti, I.; Segarra-Martí, J.; Omachi, J.; Dapor, M.; Taioli, S.; et al. UV-Light-Induced Vibrational Coherences: The Key to Understand Kasha Rule Violation in trans-Azobenzene. *J. Phys. Chem. Lett.* **2018**, 9, 1534–1541.
- (27) Punwong, C.; Owens, J.; Martínez, T. J. Direct QM/MM Excited-State Dynamics of Retinal Protonated Schiff Base in Isolation and Methanol Solution. *J. Phys. Chem. B* **2015**, 119, 704–714.
- (28) Fried, S. D.; Boxer, S. G. Electric Fields and Enzyme Catalysis. *Annu. Rev. Biochem.* **2017**, 86, 387–415.
- (29) Fried, S. D.; Bagchi, S.; Boxer, S. G. Extreme electric fields power catalysis in the active site of ketosteroid isomerase. *Science* **2014**, 346, 1510.
- (30) Cembran, A.; Bernardi, F.; Olivucci, M.; Garavelli, M. The retinal chromophore/chloride ion pair: Structure of the photoisomerization path and interplay of charge transfer and covalent states. *Proc. Natl. Acad. Sci. U. S. A.* **2005**, 102, 6255.
- (31) Romei, M. G.; Lin, C.-Y.; Mathews, I. I.; Boxer, S. G. Electrostatic control of photoisomerization pathways in proteins. *Science* **2020**, 367, 76.
- (32) Martínez, T. J. Insights for Light-Driven Molecular Devices from Ab Initio Multiple Spawning Excited-State Dynamics of Organic and Biological Chromophores. *Acc. Chem. Res.* **2006**, 39, 119–126.
- (33) Sellner, B.; Ruckebauer, M.; Stambolić, I.; Barbatti, M.; Aquino, A. J. A.; Lischka, H. Photodynamics of Azomethane: A Nonadiabatic Surface-Hopping Study. *J. Phys. Chem. A* **2010**, 114, 8778–8785.
- (34) Ruckebauer, M.; Barbatti, M.; Müller, T.; Lischka, H. Nonadiabatic Excited-State Dynamics with Hybrid ab Initio Quantum-Mechanical/Molecular-Mechanical Methods: Solvation of the Pentadieniminium Cation in Apolar Media. *J. Phys. Chem. A* **2010**, 114, 6757–6765.
- (35) Barbatti, M.; Aquino, A. J. A.; Lischka, H. The UV absorption of nucleobases: semi-classical ab initio spectra simulations. *Phys. Chem. Chem. Phys.* **2010**, 12, 4959–4967.
- (36) Ruckebauer, M.; Barbatti, M.; Müller, T.; Lischka, H. Nonadiabatic Photodynamics of a Retinal Model in Polar and Nonpolar Environment. *J. Phys. Chem. A* **2013**, 117, 2790–2799.
- (37) Siddique, F.; Barbatti, M.; Cui, Z.; Lischka, H.; Aquino, A. J. A. Nonadiabatic Dynamics of Charge-Transfer States Using the Anthracene–Tetracyanoethylene Complex as a Prototype. *J. Phys. Chem. A* **2020**, 124, 3347–3357.
- (38) Becke, A. D. Density-Functional Exchange-Energy Approximation with Correct Asymptotic-Behavior. *Phys. Rev. A* **1988**, 38, 3098–3100.
- (39) Lee, C. T.; Yang, W. T.; Parr, R. G. Development of the Colle-Salvetti Correlation-Energy Formula into a Functional of the Electron-Density. *Phys. Rev. B* **1988**, 37, 785–789.
- (40) Becke, A. D. A new mixing of Hartree–Fock and local density-functional theories. *J. Chem. Phys.* **1993**, 98, 1372–1377.
- (41) Martínez, L.; Andrade, R.; Birgin, E. G.; Martínez, J. M. PACKMOL: A package for building initial configurations for molecular dynamics simulations. *J. Comput. Chem.* **2009**, 30, 2157–2164.
- (42) Wang, J.; Wolf, R. M.; Caldwell, J. W.; Kollman, P. A.; Case, D. A. Development and testing of a general amber force field. *J. Comput. Chem.* **2004**, 25, 1157–1174.
- (43) Wang, J.; Wang, W.; Kollman, P. A.; Case, D. A. Automatic atom type and bond type perception in molecular mechanical calculations. *J. Mol. Graphics Modell.* **2006**, 25, 247–260.
- (44) Bayly, C. I.; Cieplak, P.; Cornell, W.; Kollman, P. A. A well-behaved electrostatic potential based method using charge restraints for deriving atomic charges: the RESP model. *J. Phys. Chem.* **1993**, 97, 10269–10280.
- (45) Ufimtsev, I. S.; Martínez, T. J. Quantum Chemistry on Graphical Processing Units. 3. Analytical Energy Gradients, Geometry Optimization, and First Principles Molecular Dynamics. *J. Chem. Theory Comput.* **2009**, 5, 2619–2628.
- (46) Titov, A. V.; Ufimtsev, I. S.; Luehr, N.; Martínez, T. J. Generating Efficient Quantum Chemistry Codes for Novel Architectures. *J. Chem. Theory Comput.* **2013**, 9, 213–221.
- (47) Seritan, S.; Bannwarth, C.; Fales, B. S.; Hohenstein, E. G.; Kokkila-Schumacher, S. I. L.; Luehr, N.; Snyder, J. W.; Song, C.; Titov, A. V.; Ufimtsev, I. S.; et al. TeraChem: Accelerating electronic structure and ab initio molecular dynamics with graphical processing units. *J. Chem. Phys.* **2020**, 152, 224110.
- (48) Seritan, S.; Bannwarth, C.; Fales, B. S.; Hohenstein, E. G.; Isborn, C. M.; Kokkila-Schumacher, S. I. L.; Li, X.; Liu, F.; Luehr, N.; Snyder, J. W., Jr.; et al. TeraChem: A graphical processing unit-accelerated electronic structure package for large-scale ab initio molecular dynamics. *WIREs Comput. Mol. Sci.* **2021**, 11, e1494.
- (49) Eastman, P.; Friedrichs, M. S.; Chodera, J. D.; Radmer, R. J.; Bruns, C. M.; Ku, J. P.; Beauchamp, K. A.; Lane, T. J.; Wang, L.-P.; Shukla, D.; et al. OpenMM 4: A Reusable, Extensible, Hardware Independent Library for High Performance Molecular Simulation. *J. Chem. Theory Comput.* **2013**, 9, 461–469.
- (50) Grimme, S.; Antony, J.; Ehrlich, S.; Krieg, H. A consistent and accurate ab initio parametrization of density functional dispersion correction (DFT-D) for the 94 elements H–Pu. *J. Chem. Phys.* **2010**, 132, 154104.
- (51) Curchod, B. F. E.; Glover, W. J.; Martínez, T. J. SSAIMS—Stochastic-Selection Ab Initio Multiple Spawning for Efficient Nonadiabatic Molecular Dynamics. *J. Phys. Chem. A* **2020**, 124, 6133–6143.
- (52) Curchod, B. F. E.; Sisto, A.; Martínez, T. J. Ab Initio Multiple Spawning Photochemical Dynamics of DMABN Using GPUs. *J. Phys. Chem. A* **2017**, 121, 265–276.
- (53) Bassolino, G.; Sovdat, T.; Liebel, M.; Schnedermann, C.; Odell, B.; Claridge, T. D. W.; Kukura, P.; Fletcher, S. P. Synthetic Control of Retinal Photochemistry and Photophysics in Solution. *J. Am. Chem. Soc.* **2014**, 136, 2650–2658.
- (54) Shiozaki, T.; Győrffy, W.; Celani, P.; Werner, H.-J. Communication: Extended multi-state complete active space second-

order perturbation theory: Energy and nuclear gradients. *J. Chem. Phys.* **2011**, *135*, 081106.

(55) Aquilante, F.; Autschbach, J.; Carlson, R. K.; Chibotaru, L. F.; Delcey, M. G.; De Vico, L.; Fdez. Galván, I.; Ferré, N.; Frutos, L. M.; Gagliardi, L.; et al. Molcas 8: New capabilities for multiconfigurational quantum chemical calculations across the periodic table. *J. Comput. Chem.* **2016**, *37*, 506–541.

(56) Fujino, T.; Arzhantsev, S. Y.; Tahara, T. Femtosecond Time-Resolved Fluorescence Study of Photoisomerization of trans-Azobenzene. *J. Phys. Chem. A* **2001**, *105*, 8123–8129.

(57) Lednev, I. K.; Ye, T. Q.; Matousek, P.; Towne, M.; Foggi, P.; Neuwahl, F. V. R.; Umapathy, S.; Hester, R. E.; Moore, J. N. Femtosecond time-resolved UV-visible absorption spectroscopy of trans-azobenzene: dependence on excitation wavelength. *Chem. Phys. Lett.* **1998**, *290*, 68–74.

(58) Chang, C.-W.; Lu, Y.-C.; Wang, T.-T.; Diau, E. W.-G. Photoisomerization Dynamics of Azobenzene in Solution with S1 Excitation: A Femtosecond Fluorescence Anisotropy Study. *J. Am. Chem. Soc.* **2004**, *126*, 10109–10118.

(59) Fujino, T.; Tahara, T. Picosecond Time-Resolved Raman Study of trans-Azobenzene. *J. Phys. Chem. A* **2000**, *104*, 4203–4210.

(60) Nägele, T.; Hoche, R.; Zinth, W.; Wachtveitl, J. Femtosecond photoisomerization of cis-azobenzene. *Chem. Phys. Lett.* **1997**, *272*, 489–495.

(61) Lednev, I. K.; Ye, T.-Q.; Hester, R. E.; Moore, J. N. Femtosecond Time-Resolved UV–Visible Absorption Spectroscopy of trans-Azobenzene in Solution. *J. Phys. Chem.* **1996**, *100*, 13338–13341.

(62) Satzger, H.; Spörlein, S.; Root, C.; Wachtveitl, J.; Zinth, W.; Gilch, P. Fluorescence spectra of trans- and cis-azobenzene – emission from the Franck–Condon state. *Chem. Phys. Lett.* **2003**, *372*, 216–223.

(63) Tan, E. M. M.; Amirjalayer, S.; Smolarek, S.; Vdovin, A.; Zerbetto, F.; Buma, W. J. Fast photodynamics of azobenzene probed by scanning excited-state potential energy surfaces using slow spectroscopy. *Nat. Commun.* **2015**, *6*, 5860.

(64) Schmitt, U. W.; Voth, G. A. The computer simulation of proton transport in water. *J. Chem. Phys.* **1999**, *111*, 9361–9381.

(65) Habershon, S.; Manolopoulos, D. E.; Markland, T. E.; Miller, T. F. Ring-Polymer Molecular Dynamics: Quantum Effects in Chemical Dynamics from Classical Trajectories in an Extended Phase Space. *Annu. Rev. Phys. Chem.* **2013**, *64*, 387–413.

(66) Liang, R.; Liu, F.; Martínez, T. J. Nonadiabatic Photodynamics of Retinal Protonated Schiff Base in Channelrhodopsin 2. *J. Phys. Chem. Lett.* **2019**, *10*, 2862–2868.

(67) Weingart, O.; Altoe, P.; Stenta, M.; Bottone, A.; Orlandi, G.; Garavelli, M. Product formation in rhodopsin by fast hydrogen motions. *Phys. Chem. Chem. Phys.* **2011**, *13*, 3645–3648.

(68) El-Tahawy, M. M. T.; Nenov, A.; Weingart, O.; Olivucci, M.; Garavelli, M. Relationship between Excited State Lifetime and Isomerization Quantum Yield in Animal Rhodopsins: Beyond the One-Dimensional Landau–Zener Model. *J. Phys. Chem. Lett.* **2018**, *9*, 3315–3322.